Available online at www.sciencedirect.com
SCIENCE DIRECT®
International Journal of Heat and Mass Transfer 47 (2004) 3403–3413
International Journal of HEAT and MASS TRANSFER
www.elsevier.com/locate/ijhmt

Effects of anisotropy and solid/liquid thermal conductivity ratio on flow instabilities during inverted Bridgman growth

J. Kaenton [a], E. Semma [b], V. Timchenko [c], M. El Ganaoui [d], E. Leonardi [c,*], G. de Vahl Davis [c]

[a] Khon Kaen University, Khon Kaen 40002, Thailand
[b] L3M, Université d'Aix-Marseille II/CNRS, 38 Joliot Curie, 13451 Marseille, France
[c] School of Mechanical Engineering, The University of New South Wales, Sydney, NSW 2052, Australia
[d] Université de Limoges/CNRS-UMR 6638, 123 Albert Thomas, 87000 Limoges, France

Received 19 August 2003; received in revised form 16 January 2004
Available online 25 March 2004

Abstract

The effects of a range of solid/liquid conductivity ratios on convection and flow during solidification of pure gallium in an inverted Bridgman apparatus have been investigated. A variety of steady and unsteady flow patterns, both symmetric and asymmetric, were observed and compared to available spectral results. Transition Rayleigh number values have been identified. The effects of anisotropy in thermal conductivity of gallium on the flow patterns were included. The computational method based on a fixed grid enthalpy formulation has been extended to model convection and anisotropic conduction during directional solidification.

Keywords: Directional solidification; Flow instability; Anisotropic conduction; Inverted Bridgman apparatus

1. Introduction

In crystal growth processes for producing semiconductor materials, thermal convection plays a very important role by affecting heat and mass transfer and therefore the distribution of solute. Instabilities of the flow in the melt can cause the appearance of temperature oscillations and influence the interface velocity. This in turn can lead to morphological instabilities of the plane front during directional solidification. In addition, asymmetric flow patterns can lead to an inhomogeneous structure of the growing crystal.

The vertical Bridgman configuration is one of the commonly used methods for the growth of semiconductor crystals. Two-dimensional studies of the fluid domain with a flat interface have been made by McFadden and Coriell [1], Impey and Riley [2], Phanikumar [3], Alexander et al. [4], for predictive investigation of directional solidification. These studies included configurations based on thermal or solutal control, depending on the orientation of the gravity field and the thermal and solutal gradients, and included both full and low gravity conditions. It was shown that temperature gradients parallel to the buoyancy force could induce a thermally instability, which is often employed as a model to investigate instabilities in non-isothermal fluid [5].

Symmetry-breaking flow transitions during directional solidification in both a normal vertical Bridgman system, where the hot zone lies above the crystal, and an inverted Bridgman configuration, for which the melt is below the crystal, were studied by Larroudé et al. [6]. With increasing Rayleigh number (*Ra*) in the inverted Bridgman configuration, a progressive transition was

* Corresponding author. Tel.: +61-29-385-4252; fax: +61-29-663-1222.
E-mail address: e.leonardi@unsw.edu.au (E. Leonardi).

0017-9310/$ - see front matter © 2004 Elsevier Ltd. All rights reserved.
doi:10.1016/j.ijheatmasstransfer.2004.01.017

Nomenclature

A	aspect ratio, L/W
c_p	specific heat at constant pressure
D	domain
f	volume fraction
g	gravity acceleration
h	enthalpy
h_f	latent heat
H	ampoule height
k	thermal conductivity
K	permeability
L	ampoule length
p	pressure
Pr	Prandtl number, $c_p\mu/\lambda$
Ra	Rayleigh number,
s	interface location
t	time
T	temperature
T_m	melting temperature
V	velocity
u	velocity component in x direction
v	velocity component in y direction
W	ampoule width
x, y	physical coordinates
X, Y	crystal principal coordinates

Greek symbols

α	thermal diffusivity
β_T	thermal expansion coefficient
Δx	mesh size in x direction
Δy	mesh size in y direction
Δt	time step
ε	deviation from T_m
ζ	vorticity
ϕ	interface angle with x-axis
γ	angle between crystal and physical axes
μ	dynamic viscosity
v	kinematic viscosity
ρ	density
ψ	stream function
ω	frequency

Subscripts

a	anisotropic
c	cold
h	hot
i	interface
i, j	grid point
l	liquid
min	minimum value
max	maximum value
s	solid

Superscript

$'$	dimensional quantities

observed from steady symmetry with two counter-rotating cells (SS) to steady asymmetry with one dominant cell (SAS), then to periodic motion with one (P1) or more than one frequency (P2) and finally to a quasi-periodic (QP) and non-periodic regime (NP). El Ganaoui [7] validated his results on the threshold of transitions from symmetric to periodic flow obtained using a finite volume approximation by comparison with highly accurate spectral results obtained by Larroudé et al. [6] and determined the sensitivity of the results to the mesh size. El Ganaoui et al. [8] showed that refinement of the mesh near the walls allowed the finite volume approximation to reach spectral accuracy.

Three-dimensional bifurcations of a partially melted or solidified material in a cylinder heated from below (corresponding to the inverted Bridgman configuration) were analyzed by Lan and Wang [9]. As the interface was allowed to deform, the bifurcation behavior was observed to change significantly, affecting both the onset of instability and its convective mode. The authors concluded that instability of the flow in the melting zone strongly depends on the interface deformation and therefore can be considerably affected by heat and mass transfer at the interface.

One of the important factors determining the heat transfer at the interface is the ratio between the thermal conductivities in the solid and liquid zones. The variation of liquid and solid thermal conductivities has a significant effect on the heat transfer, the interface shape and convection in the melt during directional solidification in the vertical Bridgman configuration, as was shown in Timchenko et al. [10].

In this work we study transition flow regimes for different solid/liquid thermal conductivity ratios for the solidification of gallium in an inverted vertical Bridgman configuration. Two computational models, one based on primitive variables coupled to a finite volume method and the other on the vorticity–stream function formulation coupled to a finite difference method have been used. The single phase domain corresponding to the liquid zone in the two phase system has been considered here, in order to investigate the effect of the interface on the flow instability and to compare thresholds of instability with spectral results, as well as the two phase domain containing both liquid and solid.

Gallium is a highly anisotropic material: its thermal conductivities for each crystal axis of the solid are 40.82, 88.47 and 15.99 W/m K [11]. Therefore, anisotropic heat

conduction has a major effect on solidification rate and interface morphology during conduction and convection–conduction phase change [12,13].

To study the effects of anisotropy on the transition flow regimes for different solid/liquid thermal conductivity ratios, the numerical study of anisotropy in the presence of natural convection during solidification [14] has been extended and applied to the inverted vertical Bridgman configuration. A fixed grid enthalpy formulation modified to model two-dimensional convection and anisotropic conduction during solidification of pure gallium has been used.

2. Problem definition

The inverted Bridgman growth (Fig. 1a) of a crystal of pure gallium is considered. The configuration consists of a vertical ampoule heated from below at temperature T'_h and cooled from above at T'_c. The lateral walls in the hot zone (at T'_h), and the cold zone (at T'_c) are separated by an adiabatic zone (of length $L_{\Delta T} = y'_h - y'_c$) which we consider to be stationary. The interface position is initially at the mid-height of the cavity ($y' = L/2$). The liquid is assumed to be incompressible, Newtonian and to have constant properties; the Boussinesq approximation is taken. The thermal conductivities, although constant, may be the same or different between the solid and liquid phases. All four walls are non-slip. The gravitational axis is vertically down. A prime denotes a variable with dimensions. The problem can be non-dimensionalized using W, the width of the cavity, as the scale factor for length; and W^2/α and $\rho\alpha^2/W^2$ (where α is the liquid thermal diffusivity) as the scaling factors for time and pressure. The non-dimensional temperature is $T = (T' - T'_c)/(T'_h - T'_c)$. The problem has been solved in the domain $D = [0,1] \times [0,A]$, where $A = L/W$ is the aspect ratio of the physical domain, L_l is the height of liquid and L_s is the height of the solid zone. The restricted fluid domain is obtained by considering only the liquid zone ($L_s = 0$) with a flat interface maintained at $T = T_m$, the melting temperature of the crystal (Fig. 1b).

3. Primitive variable formulation (Model 1)

For the liquid phase, the time-dependent primitive variable equations can be written in dimensionless form as:

Continuity equation: $$\nabla \cdot \boldsymbol{V} = 0 \tag{1}$$

Momentum equation:

$$\frac{\partial u}{\partial t} + (\boldsymbol{V} \cdot \nabla)u = -\nabla p + Pr\nabla^2 \boldsymbol{V} + RaPr\frac{\boldsymbol{g}}{\|\boldsymbol{g}\|}T \tag{2}$$

Energy equation: $$\frac{\partial h}{\partial t} + \nabla \cdot (\boldsymbol{V}h) = \nabla \cdot (\mathbf{k}\nabla T) \tag{3}$$

in which $\boldsymbol{V}$ is the velocity vector, p is the pressure, and $\boldsymbol{g}$ is the unit gravitational acceleration vector. The

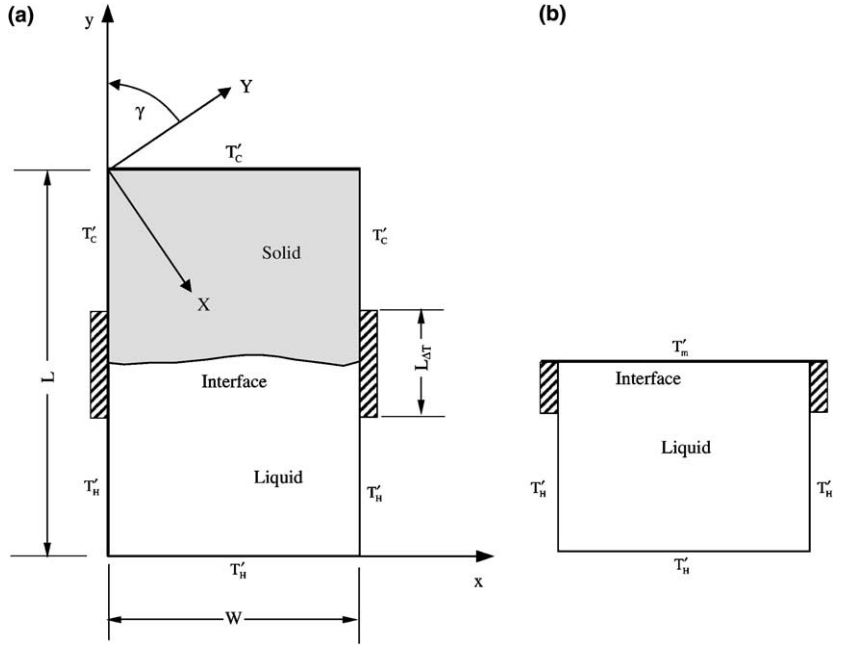

Fig. 1. Physical models: (a) inverted vertical Bridgman configuration (full cavity), (b) the restricted fluid domain.

Rayleigh number is $Ra = g\beta_T(T'_h - T'_c)W^3/\alpha\nu$, and the Prandtl number is $Pr = \nu/\alpha$, where β_T is the thermal expansion coefficient. The density, ρ, and specific heat, c_p, are assumed to be equal in the liquid and solid phases.

To solve a phase change problem, a fixed grid (enthalpy method) approach is used. The solidification takes place in the central zone ($L_{\Delta T}$) over a temperature range $T_m \pm \varepsilon$, where ε is a small quantity (typically 5% of T_m). The principle of the enthalpy method is to separate the sensible and latent heat components in the vicinity of the solid–liquid interface ($T_m - \varepsilon < T < T_m + \varepsilon$). The latent heat component is expressed in term of latent heat and liquid fraction, f_l, which is defined as:

$$\begin{aligned} &\text{for } T > T_m + \varepsilon: \quad f_l = 1 \\ &\text{for } T < T_m - \varepsilon: \quad f_l = 0 \\ &\text{for } T_m - \varepsilon < T < T_m + \varepsilon: \quad f_l = (T - T_m + \varepsilon)/2\varepsilon \end{aligned} \tag{4}$$

Using this definition of liquid fraction, the enthalpy becomes a continuous and piecewise linear function and can be written:

$$h = T + f_l Ste^{-1} \tag{5}$$

where the Stefan number is $Ste = c_p(T'_h - T'_c)/h_f$ and h_f is the latent heat of fusion. f_l is the local liquid volume fraction. An average conductivity is defined as $k = f_l k_l + (1 - f_l)k_s$ and the dimensionless energy equation takes the following form

$$\frac{\partial T}{\partial t} + \boldsymbol{V}\cdot\nabla T - a(f_l, k_R)\nabla^2 T + Ste^{-1}\frac{\partial f_l}{\partial t} = 0 \tag{6}$$

where $a(f_l, k_R) = f_l + (1 - f_l)k_R$ ($k_R = k_s/k_l$). If Ste^{-1} goes to 0 and $k_R = 1$, Eq. (6) reverts to the classical single phase energy equation.

In the momentum equations a permeability term is introduced using the Kozeny–Carman formulation [8] relation

$$K = K_0 f_l^3/(1 - f_l)^2 \tag{7}$$

and the x momentum equation becomes

$$\frac{\partial u}{\partial t} + \boldsymbol{V}\cdot\nabla u + \nabla p - Pr\nabla^2 u - RaPr\frac{\boldsymbol{g}}{\|\boldsymbol{g}\|}T + \frac{Pr}{W^2}K^{-1}u = 0 \tag{8}$$

The parameter K, which varies between infinity in the liquid and 0 in the solid, causes the velocity to become zero in the solid, i.e. as f_l approaches zero. In the fluid domain the term $K^{-1}u$ becomes zero and Eq. (8) reverts to a standard Navier–Stokes equation.

For the numerical approximation, the spatial discretization uses a finite volume method. The convective terms are evaluated using the Quadratic Upwind Interpolation for Convective Kinematics scheme QUICK with ULTRA SHARP limiter [15] to take into account high gradients in the solution. Diffusive terms are approximated using a second order centered scheme. The linear systems are solved with the classical Tridiagonal Matrix Algorithm (TDMA). The time discretization uses a second order Euler scheme. The pressure–velocity coupling is solved using the PISO algorithm. Grid dependency has been studied; we have used a grid with $\max(\Delta x, \Delta y) \leqslant 1/32$. The time step used was $\Delta t < 10^{-4}$.

4. Vorticity–stream function formulation (Model 2)

4.1. Isotropic conduction

In Model 2 the time-dependent primitive variable equations are converted into the vorticity–stream function (ζ–ψ) formulation in the conventional way, resulting in vorticity transport and stream function equations:

$$\frac{\partial \zeta}{\partial t} = -\nabla\cdot(\boldsymbol{V}\zeta) - RaPr(\nabla T \times \boldsymbol{g}) + Pr\nabla^2\zeta \tag{9}$$

$$\nabla^2\psi = -\zeta \tag{10}$$

where ζ is the vorticity and ψ is the stream function.

A finite difference method was employed, extending Tacke's method [16] to handle the discontinuous temperature and velocity gradients at the solid–liquid interface. This method removes oscillations in temperature and provides a good numerical stability in spite of the discontinuity in the temperature gradient at the solid–liquid interface. The interface location is used to calculate the actual gradients of the temperature. In two-dimensional solidification problems, Tacke's discretization was used for heat conduction in the direction of solidification while the standard discretization was used in the transverse direction [17]. This simplification is valid because, in directional solidification, the interface angle ϕ with the x-axis is normally much less than 45°.

The vorticity, stream function and velocity were set to zero in the solid. Thus their gradients are also discontinuous at the solid–liquid interface. For the convection and diffusion terms in the direction of solidification, Tacke's method was modified by the use of a non-uniform mesh for the first grid point in the liquid region. The artificial grid point used as a boundary point is located at the solid–liquid interface, i.e. $T_I = T_m$, $u_I = v_I = \psi_I = 0$. The vorticity at the interface can be found from

$$\zeta_I = -\left[1 + \left(\frac{\partial s}{\partial x}\right)^2\right]\frac{\partial^2\psi}{\partial y^2} \tag{11}$$

where s is the location of the solid–liquid interface. The boundary condition $\psi = 0$ was used for the stream

function equation. The central difference scheme was used to approximate the convection and diffusion terms.

The use of the improved discretization approach requires knowledge of the interface location at each time step. The solid–liquid interface is tracked with the use of an interface energy-balance equation [18].

$$\frac{\partial s}{\partial t} = \frac{Ste}{\sin^2\phi}\left[\left(k\frac{\partial T}{\partial y}\right)_s - \left(k\frac{\partial T}{\partial y}\right)_l\right] \quad \text{at } y = s(x,t) \tag{12}$$

Once the location of the interface is found, the liquid fraction is calculated using the assumption of a planar interface, inclined at an angle ϕ, in each computational control volume (Fig. 2). This is a reasonable assumption in directional solidification. ϕ is approximated by linear interpolation between two adjacent interface points in the x direction:

$$\phi = \tan^{-1}\left(\frac{2\Delta x}{\Delta s}\right) = \tan^{-1}\left(\frac{x_{j+1} - x_{j-1}}{s_{j+1} - s_{j-1}}\right) \tag{13}$$

where Δx is the grid size in the x direction and Δs is the difference of interface location between the two adjacent grid points [14].

The system of discretized equations was solved iteratively at each time step with a Samarskii–Andreyev ADI scheme modified to contain internal iterations [19]; a semi-implicit (Crank–Nicolson) time marching scheme was used.

4.2. Anisotropic conduction

We consider an orthorhombic crystal, gallium, with principal coordinates X and Y oriented at some angle γ to the physical coordinates x and y as shown in Fig. 1. By transforming axes from the crystal to the physical frame, relationships between (k_{11}, k_{22}), the thermal conductivities of the crystal, and $(k_{yy}, k_{xx}, k_{yx}, k_{xy})$, the conductivities of the system along the computational axes, can be determined:

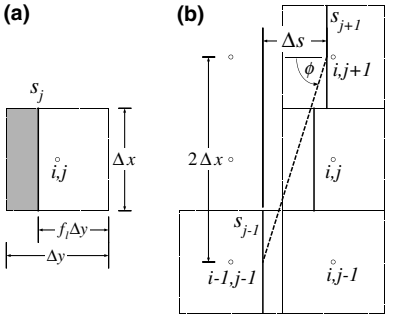

Fig. 2. Definitions of (a) liquid fraction f_l and (b) interface angle ϕ for a control volume i, j.

$$\begin{aligned} k_{yy} &= k_{11}\cos^2\gamma + k_{22}\sin^2\gamma \\ k_{xx} &= k_{11}\sin^2\gamma + k_{22}\cos^2\gamma \\ k_{xy} &= k_{yx} = (k_{22} - k_{11})\cos\gamma\sin\gamma \\ \begin{bmatrix} k_{11} & 0 \\ 0 & k_{22} \end{bmatrix}_{Y-X} &\Rightarrow \mathbf{k} = \begin{bmatrix} k_{yy} & k_{yx} \\ k_{xy} & k_{xx} \end{bmatrix}_{y-x} \end{aligned} \tag{14}$$

Since a two-dimensional model is being considered, k_{11}, k_{22} can be any two of [40.82, 88.47, 15.99] W/m K. The conduction term of the energy equation for an anisotropic material is

$$\nabla\cdot(\mathbf{k}\nabla T) = \frac{\partial}{\partial y}\left(k_{yy}\frac{\partial T}{\partial y} + k_{yx}\frac{\partial T}{\partial x}\right) + \frac{\partial}{\partial x}\left(k_{xx}\frac{\partial T}{\partial x} + k_{xy}\frac{\partial T}{\partial y}\right) \tag{15}$$

The adiabatic boundary condition at $x = 0$ or W for an anisotropic material is

$$k_{xx}\frac{\partial T}{\partial x} + k_{xy}\frac{\partial T}{\partial y} = 0 \tag{16}$$

where $k_{xy}\frac{\partial T}{\partial y}$, the heat flow in the x direction driven by a temperature gradient in the z direction, is a transverse heat flux introduced by anisotropic conduction. k_{xy} will be zero for $\gamma = 0°$ and 90°, or for isotropic conduction $(k_{11} = k_{22})$. Isotropic conduction is assumed in the liquid with $k_l = 33.67$ W/m K.

For analysis, a theoretical interface angle ϕ_t can be approximated from the slope of the isotherms in the solid at the adiabatic walls, using the boundary condition (16).

$$-\frac{k_{xx}}{k_{xy}} = \frac{\partial T/\partial y}{\partial T/\partial x} = \frac{\partial x}{\partial y} \cong \tan\phi_t \tag{17}$$

where the second equality is obtained by application of the chain rule [18].

The performance of the present method was examined and validated by comparing computational results with the experimental results of Gau and Viskanta [12,13] on the morphology and positions of the interface [14].

5. Results and discussion

In the general formulation, the non-dimensional parameters which define the problem to be solved are Ra, Pr, A, L_s/L_l, k_R. For the present study Prandtl number has been fixed to 0.01 to allow us to concentrate on the dependency of the dynamic regime on Ra and on the presence of the interface. L_s/L_l has been fixed to 0 or 1 (i.e. $A = 1$ for a single phase model and $A = 2$ for the full model with phase change). These aspect ratios offer a good compromise in terms of spatial resolution, time step and computational cost [6] and also allow us to make comparisons with available spectral results. The

classification of flow regimes proposed by Larroudé et al. [6] (presented in Section 1) is used. A number of characteristic variables are used to analyze the flow regime: $\psi_{max}(t) = \max(\psi(x,t), x \in D)$, $\psi_{min}(t) = \min(\psi(x,t), x \in D)$. The value of time step varies from 5×10^{-5} to 5×10^{-4} to ensure a good representation of unsteady flow. For steady solutions the symmetry will be quantified by using $\delta\psi = |\psi_{max}| - |\psi_{min}|$.

5.1. Restricted fluid domain ($L_s = 0$)

Calculations have been made for the restricted fluid domain shown in Fig. 1b. A mesh validation study was first undertaken, at $Ra = 10^4$. The results are shown in Table 1, on the basis of which a mesh of 81×81 with grid refined near the walls was used for these calculations.

Transitions from steady symmetrical to aperiodic solutions have been studied using the primitive variable formulation Model 1 and the derived variable Model 2 for Rayleigh numbers in the range $0 \leqslant Ra \leqslant 4\times10^5$. Fig. 3 compares the results (isotherms and streamlines) obtained with the two models for $Ra = 10^4$. The agreement is excellent; for example $\psi_{max} = 0.6638$ (Model 1) and $\psi_{max} = 0.6627$ (Model 2). The symmetrical configuration is composed of two counter-rotating cells in which the fluid rises in the center of the cavity towards the cold wall (which corresponds to the interface in the two phase system); the stream function exhibits two extreme values, negative and positive.

Table 1
Mesh validation

Mesh	ψ_{max}	ψ_{min}	$\Delta\psi_{max}/\psi_{max}$	$\Delta\psi_{min}/\psi_{min}$
41×41	1.7137	−0.08878	5.24%	3.05%
64×64	1.7866	−0.08675	1.21%	0.70%
81×81	1.8025	−0.08631	0.33%	0.18%
124×124	1.8085	−0.08615	–	–

The first observed transition characterizes the steady flow and corresponds to transition from SS to SAS for $Ra \sim 10^4$. Note that the conditions in Larroudé et al. [6] are slightly different from present investigations, in that a translation of the ampoule with a non-dimensional speed $U_t = 5\times10^{-3}$ was imposed. There is a linear effect on the stream function, for $Ra = 4000$, $\psi_{max} = 0.270$ which is close to present calculations ($\psi_{max} = 0.290$ for Model 1).

For $10^4 \leqslant Ra \leqslant 3\times10^4$, an asymmetric SAS solution develops, with one cell growing preferentially from one of the two cells of the SS solution. The flow bifurcates between two steady branches from SS to SAS after a period of non-dimensional time close to $t = 20$. This behavior is consistent with the calculations of Larroudé et al. [6] showing the transition from one steady state to another and convergence to SAS dominated by a one-cell flow. Fig. 4 illustrates this situation with the temporal evolution of the temperature in the point close to the bottom hot wall indicating the original symmetric solution followed by an asymmetric two-cell solution and the final asymmetric one-cell solution.

The next transition, to oscillatory flow, is reached around $Ra = 3.5\times10^4$ and leads to a periodic solution with a dimensionless frequency $\omega = 6.67$. The asymmetric solution is retained with the same flow structure dominated by a one-cell flow varying from a quasi-circular shape to a deformed shape. The frequency of the oscillations increases with Ra as shown in Fig. 5. Increasing Ra to 1.9×10^5, the flow becomes P2 characterized by ω and $\omega/2$ ($\omega = 33.33$). The aperiodic regime which starts around $Ra = 3.5\times10^5$ is characterized by a complex non-periodic oscillation.

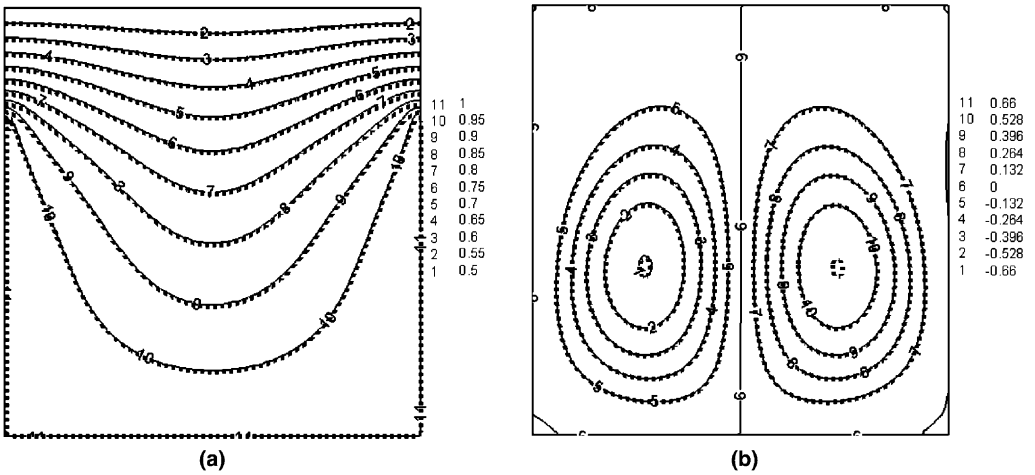

Fig. 3. Isotherms and streamlines for the restricted fluid domain SS solution ($Ra = 10^4$), Model 1 (solid line) and Model 2 (dashed line).

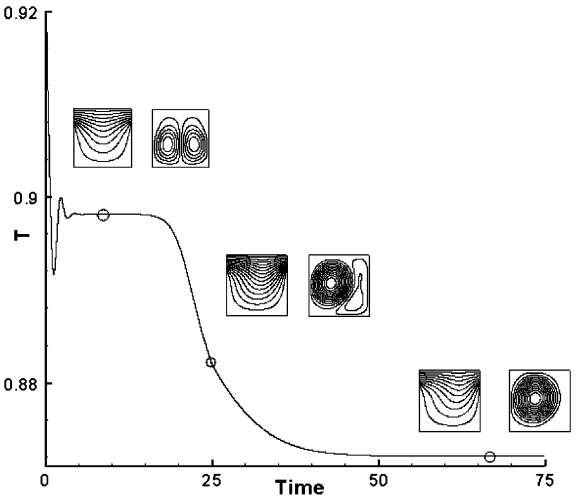

Fig. 4. Transition from SS to SAS solution for $Ra \sim 10^4$.

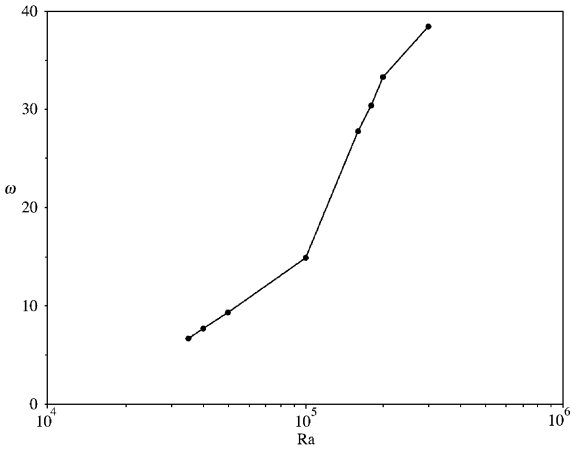

Fig. 5. Periodic regime: variation of the frequency of the oscillations of ψ_{max} versus Ra.

5.2. Full cavity (isotropic case)

In this section results for the full model with phase change are presented. The height of the liquid zone was chosen to be equal the height of the solid zone ($L_s/L_l = 1$, $A = 2$). Solutions using Model 1 were obtained with a time step $\Delta t = 5 \times 10^{-5}$ and a mesh of 80×160 refined at the adiabatic zone to account for the interface deformation and also in the horizontal direction near the walls with $x_{i+1}/x_i = 1.02$ to describe accurately the boundary layer characterizing low Pr behavior.

To investigate the effects of the deformation of the solid/liquid interface a comparison of numerical results for the restricted fluid domain and full domain containing both solid and liquid zones for $Ra = 55,500$ and $Ste^{-1} = 0$ has been undertaken. The results describing the evolution of the temperature at the point M1(0.25, 0.25) together with flow patterns and isotherms are presented in Fig. 6. Isotherms and streamlines are shown in some characteristic instants of time, particularly at chosen minimum and maximum points of the signal, designated in the figure as a1, b1 and c1 for the restricted fluid domain and a2, b2 and c2 for the full cavity. Both solutions exhibit oscillatory flow from $t = 0$. The flow in the restricted fluid domain undergoes transition to a periodic flow with a dimensionless frequency $\omega = 38.4$. For the full cavity, transition to more complex non-periodic modes occurs at about $t \sim 0.45$. The flow regime is the superposition of a periodic flow, with a frequency approximately the same as that in the restricted fluid domain, and a secondary flow introduced by the deformation of the interface. This superposition results in a complex multicellular flow.

Solutions were also obtained with both models for $Ra = 69,375$. Solutions using Model 2 were obtained with time step $\Delta t = 1.5 \times 10^{-4}$ and a mesh of 121×241. Fig. 7a shows the evolution of temperature at the point M1(0.25, 0.25). Using Model 1, the transition to a non-periodic regime is now found to occur almost immediately, at about $t \sim 0.1$. Fig. 7b shows an expanded view of the temperature history at M1 over the time interval $0.7 \leqslant t \leqslant 1.1$. The agreement between the two solutions is almost perfect.

The effects of solid/liquid conductivity ratio k_s/k_l on convection and transitions of flow regimes for both the isotropic and anisotropic cases have been studied using the vorticity–stream function formulation, Model 2.

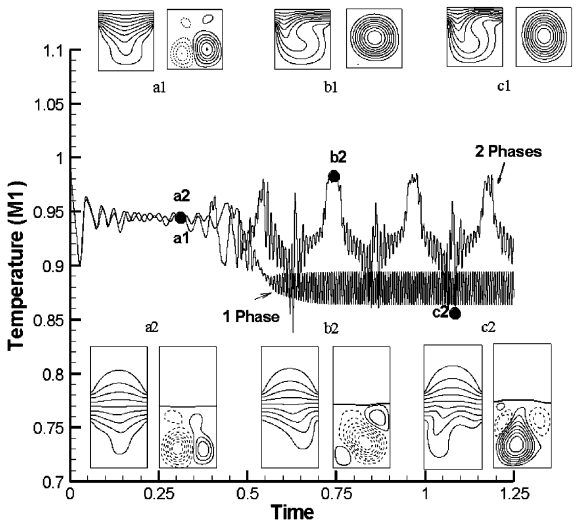

Fig. 6. Temperature evolution in the monitoring point M1(0.25, 0.25), flow patterns and isotherms for the restricted fluid domain and full cavity configurations ($Ra = 55,500$). b1 and c1 correspond to instants of time at which maximum and minimum of periodic signal in the restricted fluid domain occur.

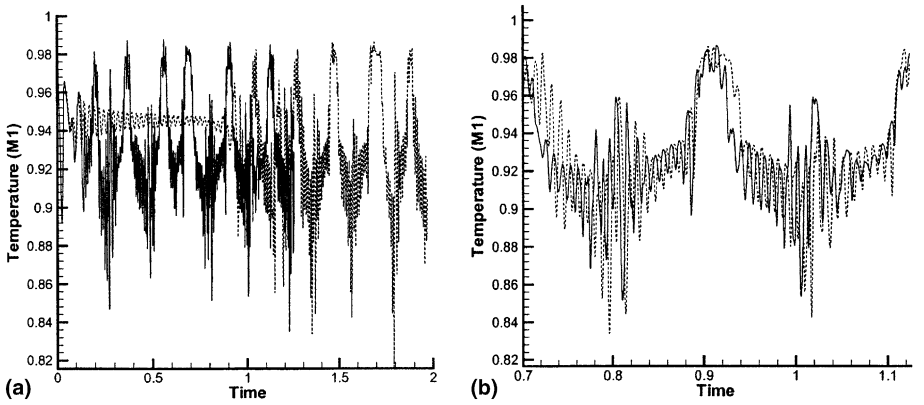

Fig. 7. Temperature evolution in the monitoring point M1(0.25, 0.25) for $Ra = 69,375$, obtained using Model 1 (solid line) and Model 2 (dashed line).

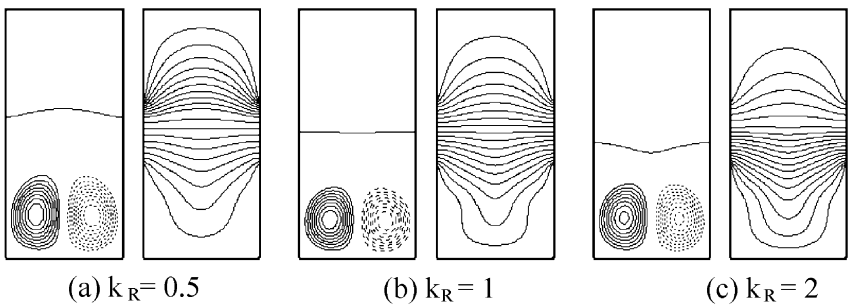

Fig. 8. Steady symmetric (SS) two-cell regime of isotropic solids (contours drawn with dashed lines are for counter-clockwise flows).

Mesh refinement studies were undertaken: a uniform mesh system of 81×161 with time step $\Delta t = 1.5 \times 10^{-4}$ was used for a solution region of aspect ratio 2. Solutions were performed in the inverted vertical Bridgman configuration (Fig. 1), with the following values of the non-dimensional parameters:

$$10^3 < Ra \leqslant 10^6 \quad Ste = 1 \quad Pr = 0.01 \quad A = 2$$
$$T_m = 0.5 \quad T_c = 0 \quad T_h = 1 \quad L_{\Delta T} = L/4.$$

We first discuss the instability of the flow regime in the melt for values of $k_R = k_s/k_l$ of 0.5, 1 and 2 when the solid is isotropic. Comparisons are presented of the nature of the flow, and of instability thresholds. Fig. 8 shows that a flat solid/liquid interface occurs for $k_R = 1$, a convex shape (viewed from the solid) is formed for $k_R < 1$, and a concave shape for $k_R > 1$. The convexity increases quasi-linearly with $\ln(k_R)$. These results are compatible with the experimental and numerical studies of Huang et al. [20] for a normal vertical Bridgman configuration (liquid above solid) subjected to the same thermal conditions as shown in Fig. 1a.

Transition flow regimes are summarized in Table 2. For $k_R = 0.5$ (Fig. 9) and $k_R = 1$ (Fig. 10), the flow bifurcates from a steady symmetric two-cell solution

Table 2
Characteristic Rayleigh numbers for the transition between flow regimes for various ratios of solid/liquid conductivity

Case	Flow regimes	*Ra* range for transition
$k_i = 0.5$	SS–NP	27,750–55,500
$k_i = 1$	SS–NP	55,500–69,375
$k_i = 2$	SS–P1	27,750–83,250

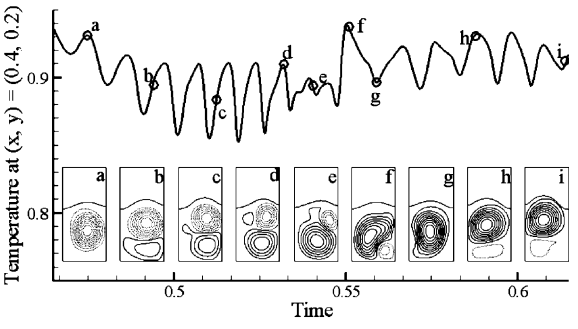

Fig. 9. Unsteady aperiodic regime: $k_R = 0.5$, $Ra = 55,500$. The letters (a–i) indicate the times at which flow patterns occur.

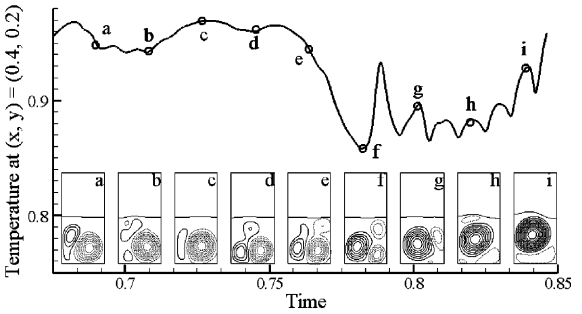

Fig. 10. Unsteady aperiodic regime: $k_R = 1.0$, $Ra = 69,375$.

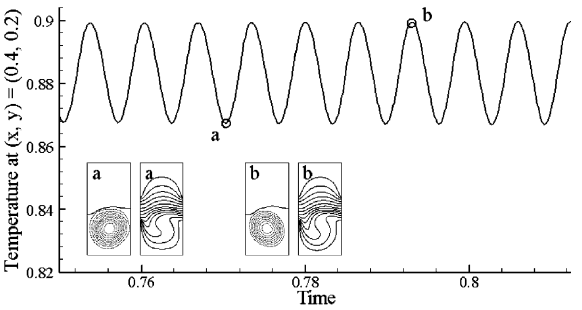

Fig. 11. Unsteady periodic regime: $k_R = 2.0$, $Ra = 41,625$.

(SS) to an unsteady aperiodic flow (NP). The interface shape changes following the time-dependent flow patterns. For $k_R = 2$ (Fig. 11), transition occurs from SS to an unsteady periodic one-cell flow (P1). Compared to Fig. 8c, the concave shape of the interface is modified to a convex shape. The unsteady periodic flow pattern is only slightly changed in one cycle.

In terms of solid/liquid interaction, planar, convex, concave and mixed (convex–concave) interfaces are observed depending on the convective regime and thermal conductivities ratio.

5.3. Full cavity (anisotropic case)

For an anisotropic solid, we selected values of [k_y/k_l, k_X/k_l: γ] as [0.5, 1: 60°], [0.5, 2: 35°] and [2, 1: 60°] for which the resulting values of k_a ($= k_{xy,s}/k_l$) are 0.875, 1 and 1.25. Anisotropy causes a non-orthogonal interface at the adiabatic side walls and therefore the flow patterns are not symmetrical (Fig. 12a–c).

Transitions were observed at a smaller Ra than in the isotropic solids (Table 3). SAS with two cells becomes P1 with two cells at $2775 < Ra < 11,100$ for $k_a = 0.875$. The periodic flow patterns become more complex with increasing Ra and change to aperiodic regimes at $11,100 < Ra < 66,600$. The developments of the periodic flow patterns during the transition are shown in Fig. 13. The transition patterns of SAS–P1 with two cells for $k_a = 1$ are similar to those for $k_a = 0.875$, but at slightly larger Ra. Interestingly, the periodic flow is diminished and SAS with one cell was observed at $13,875 < Ra < 22,200$. When Ra is increased to 27,750, a periodic multicell regime (PMC) was observed (Fig. 14). The periodic flow is very complicated with three small oscillations in one cycle. The development of the flow pattern with Ra is simple for the case of $k_a = 1.25$. The counter-clockwise cell from Fig. 12c increases in size and the clockwise cell reduces in size as Ra is increased

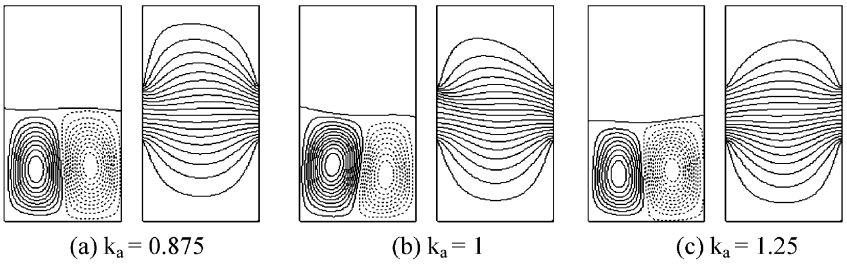

Fig. 12. Steady asymmetric (SAS) two-cell regime of anisotropic solids.

Table 3
Characteristic Rayleigh numbers for transition between different flow regimes

Case	Flow regimes	Ra range for transition
$k_a = 0.875$	SAS (2)–P1(2)–NP	2,775–11,100–33,300
$k_a = 1$	SAS (2)–P1(2)–SAS (1)–PMC–NP	2,775–13,875–22,200–27,750–41,625
$k_a = 1.25$	SAS (2)–SAS(1)–P1(1)	2,775–13,875–33,300

Number of cells is given in the brackets.

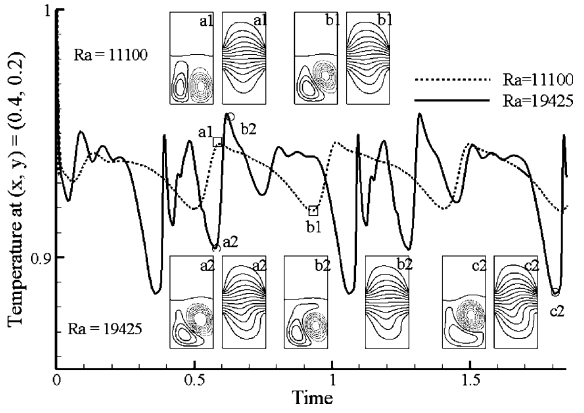

Fig. 13. Unsteady periodic two-cell regime of $k_a = 0.875$ at $Ra = 11,100$ and $Ra = 19,425$.

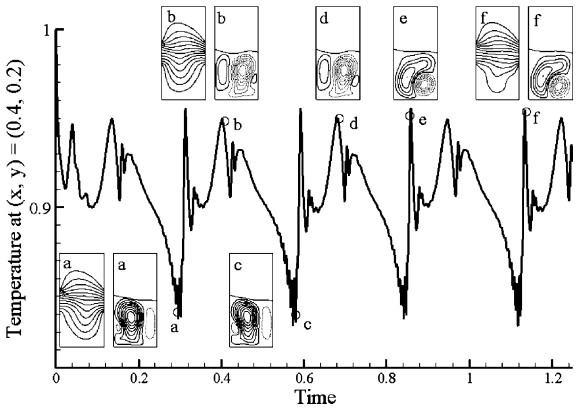

Fig. 14. Unsteady periodic multicell regime of $k_a = 1.0$ at $Ra = 27,750$.

from 2775. SAS with one cell was observed at $Ra = 13,875$ and the interface has changed from the concave to convex shape. In the range $13{,}875 < Ra < 30,525$, it remains steady but with a slightly increased convex shape (towards the solid) of the interface and increasing flow strength. SAS with one cell has a transition to P1 with one cell at $30{,}525 < Ra < 55{,}500$.

6. Conclusion

The effects of the solid/liquid thermal conductivity ratio, the interface shape and thermal anisotropy on the threshold of flow instability in the liquid zone during inverted Bridgman growth have been investigated numerically. For the single phase restricted to the liquid zone only, the results obtained in this study for transitions from steady symmetrical to unsteady periodic and aperiodic regimes are consistent with results obtained using a spectral method [6]. A very good agreement was achieved between results on the transition to complex unsteady flows obtained using two computational models: one based on primitive variables coupled to a finite volume method and another on the vorticity–stream function formulation coupled to a finite differences method.

Results show the effect of the solid/liquid interface shape on the flow regime when comparing the full model to the restricted fluid model. In the presence of the deforming interface flow pattern is changing yielding to a complex multicellular flow.

Transition flow regimes for anisotropic conduction have been studied for different solid/liquid thermal conductivity ratios during the inverted Bridgman growth. The steady two-cell patterns are symmetrical for isotropic solids but not for anisotropic solids. Anisotropic solids have transitions from steady to unsteady flow patterns at smaller values of Rayleigh number compared to isotropic solids. When anisotropic conduction in the solid is included, inclination of the interface profile at the adiabatic walls is observed.

The results show that the variation of liquid and solid thermal conductivities in both isotropic and anisotropic solids has significant effect on the heat transfer, the interface shape and flow regimes in the melt during directional solidification in the vertical Bridgman configuration.

References

[1] B. McFadden, S.R. Coriell, Thermosolutal convection during directional solidification. II. Flow transitions, Phys. Fluids 30 (1987) 659–671.
[2] M.D. Impey, D.S. Riley, A.A. Wheeler, K.H. Winetrs, Bifurcation analysis of solutal convection during directional solidification, Phys. Fluids A 3 (1991) 535.
[3] M.S. Phanikumar, Thermosolutal convection in a rectangular enclosure with strong side-walls and bottom heating, Int. J. Heat Fluid Flow 15 (4) (1994) 325–335.
[4] J.I.D. Alexander, S. Amiroudine, J. Ouazzani, F.J. Rozenberger, Analysis of the low gravity tolerance of Bridgman–Stockbarger crystal growth. II. Transient and periodic accelerations, J. Cryst. Growth 113 (1991) 21–38.
[5] S. Ostrach, Natural convection in enclosures, J. Heat Transfer 110 (1988) 1175–1190.
[6] Ph. Larroudé, J. Ouazzani, J.I.D. Alexander, P. Bontoux, Symmetry breaking flow transitions and oscillatory flows in 2D directional solidification model, Eur. J. Mech.—B/Fluids 13 (3) (1994) 353–381.
[7] M. El Ganaoui, Modélisation numérique de la convection thermique instationnaire en presence d'un front de solidification deformable, Thèses de l'Université d'Aix-Marseille, 1997.
[8] M. El Ganaoui, P. Bontoux, A. Lamazouade, E. Leonardi, G. de Vahl Davis, Computational model for solutal convection during directional solidification, Numer. Heat Transfer, Part B 41 (2002) 325–338.

[9] C.W. Lan, C.H. Wang, Three-dimensional bifurcations of a two-phase Rayleigh–Benard problem in cylinder, Int. J. Heat Mass Transfer 44 (2001) 1823–1836.
[10] V. Timchenko, M. El Ganaoui, E. Leonardi, P. Bontoux, G. de Vahl Davis, Effect of thermal conductivities on heat and mass transfer during directional solidification, in: T.A. Kowalewski, F. Stella, J. Banaszek, J. Szmyd (Eds.), Proceedings of International Workshop on Phase Change with Convection, Polish Academy of Sciences, Warsaw, Poland, 5, 1999, pp. 151–154.
[11] W.H. Cubberly, Metal Handbook, Properties and Selection: Nonferrous Alloys and Pure Metals, ninth ed., ASM, Metal Park, OH, 1979, pp. 736–737.
[12] C. Gau, R. Viskanta, Effect of crystal anisotropy on heat transfer during melting and solidification of a metal, J. Heat Transfer 107 (1985) 706–708.
[13] C. Gau, R. Viskanta, Effect of natural convection on solidification from above and melting from below of a puremetal, Int. J. Heat Mass Transfer 28 (3) (1985) 573–587.
[14] J. Kaenton, G. de Vahl Davis, E. Leonardi, S.S. Leong, A numerical study of anisotropy and convection during solidification, Numer. Heat Transfer, Part B 41 (3–4) (2002) 309–323.
[15] B.P. Leonard, S. Mokhtari, Beyond first order upwinding: the ULTRA-SHARP alternative for nonoscillatory steady-state simulation of convection, Int. J. Numer. Methods Eng. 30 (1990) 729–766.
[16] K.H. Tacke, Discretization of the explicit enthalpy method for planar phase change, Int. J. Numer. Methods Eng. 21 (1985) 543–554.
[17] J. Kaenton, G. deVahl Davis, E. Leonardi, Computation of anisotropic conduction and solidification, in: G.B. Brassington, J.C. Patterson (Eds.), Proceedings of the 7th Heat and Mass Transfer Australasian Conference, Chalkface Press Pty. Ltd., Cottesloe, Western Australia, 2000, pp. 175–180.
[18] J.A. Weaver, R. Viskanta, Effects of anisotropic heat conduction on solidification, Numer. Heat Transfer, Part A 15 (1989) 181–195.
[19] V. Timchenko, P.Y.P. Chen, E. Leonardi, G. de Vahl Davis, R. Abbaschian, A computational study of transient plane front solidification of alloys in a Bridgman apparatus under microgravity conditions, Int. J. Heat Mass Transfer 43 (2000) 963–980.
[20] C.E. Huang, D. Elwell, R.S. Feigelson, Influence of thermal conductivity of interface shape during Bridgman growth, J. Cryst. Growth 64 (1983) 441–449.